Y. Wang et al., Physical Review B 114, 175107 (2026), Supplementary Material

**Supplementary Information**

# Pressure-Induced Electronic Delocalization and Superconductivity in $GaNb_4Se_8$

Yuejian Wang[1,*], Zhongyan Wu[2], Bhupendra K C[3], Dongzhou Zhang[4], Lin Wang[2], Sanjay V. Khare[3], Lilian Prodan[5,6], Vladimir Tsurkan[5,6]

[1]Department of Physics, Oakland University, Rochester, MI 48309, USA
[2]Center for High-Pressure Science (CHiPS), State Key Laboratory of Metastable Materials Science and Technology, Yanshan University, Qinhuangdao, Hebei 066004, China
[3]Department of Physics and Astronomy, and Wright Center for Photovoltaics Innovation and Commercialization (PVIC), University of Toledo, Toledo, Ohio 43606, USA
[4]GeoSoilEnviroCARS, University of Chicago, Argonne, IL 60439, USA
[5]Experimental Physics V, Center for Electronic Correlations and Magnetism, University of Augsburg, Augsburg 86135, Germany
[6]Institute of Applied Physics, Moldova State University, MD-2028 Chisinau, Republic of Moldova

[*]Email: ywang235@oakland.edu

**Supplementary Note I**: **High-pressure Single-Crystal X-ray Diffraction**

To identify the crystal structure of the high-pressure phase, single-crystal X-ray diffraction (SCXRD) measurements were conducted at beamline 13-BM-C. A SS-80 diamond anvil cell (purchased from DACTools) equipped with two 300 μm culets was used as the pressure cell. A 200 μm-thick rhenium gasket was pre-indented to ~45 μm, and a 200 μm-diameter hole was drilled at the center of the indentation. A small single crystal (~30 μm) together with a ruby sphere (pressure calibrant) were loaded into the chamber together. Neon was loaded as the pressure-transmitting medium using the GSECARS gas-loading system [1].

The X-ray beam was monochromated to λ = 0.4306 Å with a 1 eV bandwidth using a Si(311) monochromator, and focused to a 9 μm × 11 μm (FWHM) spot by a Kirkpatrick–Baez mirror system. Diffracted intensities were recorded with a Pilatus3 1M detector (Dectris) positioned ~200 mm from the DAC. A NIST SRM 660a $LaB_6$ standard was used to calibrate the sample–to–detector distance and detector tilt. Prior to data collection, the sample was centered at the rotation axis of the diffractometer. Compression was controlled by a membrane-driven system. Diffraction patterns were collected over a 70° rotation range with 0.5° steps and 1 s exposure time per frame.

The diffraction images were integrated and processed using APEX 5 (Bruker). Intensities were scaled according to the diffracted volumes at different rotation angles. The corrected reflection intensities were used for crystal-structure refinement with Olex2, which incorporates SHELXL [2, 3].

**Supplementary Note II: Technical Details of Transport Analysis**

Following the reviewer's guidance, we have systematically evaluated the four transport mechanisms (Arrhenius, Small-polaron hopping, Mott-VRH, and ES-VRH) across the relevant temperature windows. We have also refined the localization length calculations using rigorous error propagation and softened our phrasing regarding the transport transitions. Our detailed points are addressed below:

The equations we used are:

Arrhenius: $\rho = \rho_0 \exp\left(\frac{Ea}{2k_BT}\right)$

Mott-VRH: $\rho = \rho_0 \exp\left[*\frac{T0}{T}+\frac{1}{4}\right]$

ES-VRH: $\rho = \rho_0 \exp\left[*\frac{T0}{T}+\frac{1}{2}\right]$

Small-polaron: $\rho = \rho_0 T \exp\left[\frac{Ea}{k_BT}\right]$

The above equations are linearized by taking the natural logarithm:

$$Ln(\rho) = Ln(\rho_0) + \frac{E_a}{2k_BT}$$

$$Ln(\rho) = Ln(\rho_0) + 5\frac{T_0}{T}^{0.25})$$

$$\mathrm{Ln}(\rho)=\mathrm{Ln}(\rho_0)+5\left(\frac{T_0}{T}\right)^{0.5}$$

$$Ln*\frac{\rho}{T}+=Ln(\rho_0)+\frac{E_a}{k_BT}$$

**Comprehensive Cross-Model Comparison and Goodness-of-Fit Values**

To robustly justify the selection of the Efros-Shklovskii Variable-Range Hopping (ES-VRH) model, we have comprehensively fitted our transport data using all four requested models. The corresponding parameters, including the intercept (a), slope (b), adjusted coefficient of determination ($R^2$), and reduced chi-squared ($\chi^2$_red), are summarized in the comprehensive table below:

**Table R1.** Comprehensive transport fitting parameters under various conduction models.

| Function | Data range (K) | a | b | $R^2$ | $\chi^2$_red |
|---|---|---|---|---|---|
| Arrhenius | 50-124 | -1.3183 ± 0.0505 | 851.45 ± 3.96 | 0.99981 | 0.0592559 |
| Small-polaron | 50-124 | -6.709 ± 0.087 | 929.25 ± 6.83 | 0.999528 | 0.175745 |
| ES-VRH | 220k-300 | -5.2756 ± 0.641 | 126.45 ± 10.3 | 0.937602 | 0.3586 |
| ES-VRH | below100 | -13.14 ± 0.362 | 201.85 ± 3.07 | 0.998699 | 0.206179 |
| Mott-VRH | 220k-300 | -13.191 ± 1.24 | 63.289 ± 4.96 | 0.941876 | 0.334035 |
| Mott-VRH | below 100 | -37.009 ± 1.19 | 139.01 ± 3.47 | 0.996494 | 0.555651 |

**Table R2.** Propagated physical parameters based on the ES-VRH and Mott-VRH models.

| Function | Data range (K) | $E_a$ (meV) | $T_0$ (K) | $\xi$ (Å) |
|---|---|---|---|---|
| Arrhenius | 50-124 | 146.8±0.3 | | |
| Small-polaron | 50-124 | 160.2±0.6 | | |
| ES-VRH | 220k-300k | | 15989.6±2604.9 | 2.92±0.48 |
| ES-VRH | below100k- | | 40743.4±1239.4 | 1.15±0.04 |
| Mott-VRH | 220k-300k | | $1.604\times10^7\pm0.5\times10^7$ | 0.0029±0.0009 |
| Mott-VRH | Below 100k- | | $3.734\times10^8\pm0.37\times10^8$ | 0.000125±0.000012 |

Although the Arrhenius and small-polaron models yield high mathematical $R^2$ values, they are primarily applicable to thermally activated transport in conventional semiconductors and polaronic conductors, and therefore lack a sound physical basis for describing charge transport in heavily localized cluster Mott insulators such as $GaNb_4Se_8$ at cryogenic temperatures, where charge transport is expected to be dominated by variable-range hopping between localized states rather than simple thermal activation.

Crucially, comparing the two hopping models in the low-temperature regime, ES-VRH exhibits a better fit (smaller $\chi^2$_red) compared to Mott-VRH. This strongly points to the presence of a Coulomb gap dominating the low-temperature hopping dynamics. Meanwhile, as shown in Table

R2, the Mott-VRH model yields astronomical values for $T_0$ (~$10^8$ K) and sub-atomic, physically impossible localization lengths $\xi$ (~$10^{-4}$Å).

**Calculation of the Localization Length ($\xi$)**

The localization length $\xi$, representing the spatial extent of the electronic wavefunction, is derived from $T_0$ using the following relation:

$$\xi = \frac{\beta \cdot e^2}{4\pi\epsilon_0 s_r k_B T_0} \qquad (3)$$

In our calculations, we utilize the following standard constants:

- Numerical coefficient $\beta$=**2.8**.
- Relative dielectric constant $\varepsilon_r$≈**10 [4].**
- Physical constants:

  $e$=1.602×$10^{-19}$ C, $k_B$=1.381×$10^{-23}$ J/K, and $\epsilon_0$=8.854×$10^{-12}$ F/m.

For practical computation in units of Ångströms (Å), Eq. (3) simplifies to:

$$\xi(\text{Å}) \approx \frac{467{,}600}{s \cdot T_0(K)} \qquad (4)$$

**Calculation of the Hopping Energy ($W_{ES}$)**

The average hopping energy $W_{ES}$, representing the energy barrier for a carrier jump at a specific temperature $T$, is calculated as:

$$W_{ES}(T) = 0.5 \cdot k_B \cdot A\overline{T_0 \cdot T} \qquad (5)$$

Using our fitted values, we obtain $W_{ES} \approx 87.9\ meV$ at 260 K (High-T regime) and $W_{ES} \approx 75.3\ meV$ meV at 75 K (Low-T regime).

**Supplementary References:**

[1] M. Rivers, V.B. Prakapenka, A. Kubo, C. Pullins, C.M. Holl, S.D. Jacobsen, The COMPRES/GSECARS gas-loading system for diamond anvil cells at the Advanced Photon Source, High Pressure Research, 28 (2008) 273-292.
[2] G. Sheldrick, A short history of SHELX, Acta Crystallographica Section A, 64 (2007) 112-122.
[3] O.V. Dolomanov, L.J. Bourhis, R.J. Gildea, J.A.K. Howard, H. Puschmann, OLEX2: a complete structure solution, refinement and analysis program, Journal of Applied Crystallography, 42 (2009) 339-341.
[4] R. Rösslhuber, R. Hübner, M. Dressel, A. Pustogow, Pressure-dependent dielectric response of the frustrated Mott insulator *k*-(BEDT-TTF)$_2$Ag$_2$(CN)$_3$, Physical Review B, 107 (2023) 075113.
[5] M.M. Abd-Elmeguid, B. Ni, D.I. Khomskii, R. Pocha, D. Johrendt, X. Wang, K. Syassen, Transition from Mott insulator to superconductor in $GaNb_4Se_8$ and $GaTa_4Se_8$ under high pressure, Physical Review Letters, 93 12 (2004) 126403.
[6] R. Pocha, D. Johrendt, B. Ni, M.M. Abd-Elmeguid, Crystal structures, electronic properties, and pressure-induced superconductivity of the tetrahedral cluster compounds $GaNb_4S_8$, $GaNb_4Se_8$, and $GaTa_4Se_8$, Journal of the American Chemical Society, 127 (2005) 8732-8740.

**Supplementary Table S1**. Lattice parameters of cubic $GaNb_4Se_8$ obtained from GGA calculations.

| Pressure (GPa) | Lattice constant (a) Å |
|---|---|
| 0 | 10.36,<br>10.32[a],<br>10.42[b] |
| 15 | 10.17 |

[a] Experimental Ref. [5]
[b] Experimental Ref. [6]

**Supplementary Table S2.** Helmholtz free energy (F) of cubic and orthorhombic $GaNb_4Se_8$ structures as a function of pressure at 300 K.

| Pressure (GPa) | Cubic (kJ/mol) | Orthorhombic (kJ/mol) |
|---|---|---|
| 00 | -80.62 | -61.97 |
| 05 | -59.13 | -51.27 |
| 10 | -54.70 | -39.53 |
| 15 | -50.49 | -27.91 |
| 20 | -62.66 | -25.12 |
| 25 | -49.42 | -22.24 |
| 30 | -37.96 | -21.19 |
| 35 | -28.24 | -16.95 |
| 40 | -19.91 | -13.02 |
| 45 | -12.54 | -9.60 |

**Supplementary Table S3.** Indexed X-ray diffraction peaks for the monoclinic C2 phase at 38.5 GPa obtained from Le Bail analysis, listing assigned (hkl) reflections and corresponding d-spacings.

| symmetry | Monoclinic (C2) | |
|---|---|---|
| Pressure | 38.5 GPa | |
| Lattice parameter | a: 10.82422 Å<br>c: 10.73357Å<br>b: 13.18737 Å<br>β: 100.035° | |
| HKL | position | D-spacing |
| 111 | 3.9917 | 6.1316 |
| 021 | 4.3753 | 5.5943 |
| $20\bar{1}$ | 4.770 | 5.1317 |
| 113 | 7.9130 | 3.0949 |
| 222 | 7.9883 | 3.0658 |
| $22\bar{3}$ | 8.4923 | 2.8842 |
| 240 | 8.7356 | 2.8037 |
| 042 | 8.7570 | 2.7972 |
| 150 | 9.5692 | 2.5603 |
| 420 | 9.9175 | 2.4705 |
| $42\bar{2}$ | 10.2476 | 2.3912 |
| $33\bar{3}$ | 10.5029 | 2.3332 |
| $40\bar{3}$ | 10.5196 | 2.3295 |
| 224 | 11.6583 | 2.1027 |
| $35\bar{2}$ | 12.0158 | 2.0403 |
| $51\bar{3}$ | 12.5019 | 1.9613 |
| 170 | 13.2201 | 1.8552 |
| 602 | 15.3241 | 1.6017 |
| $71\bar{1}$ | 15.9930 | 1.5351 |
| $48\bar{3}$ | 18.2632 | 1.3456 |
| 800 | 18.4467 | 1.3323 |
| $26\bar{7}$ | 19.6351 | 1.2524 |
| $41\bar{0}3$ | 21.4485 | 1.1476 |

**Supplementary Table S4.** Critical superconducting temperatures under applied magnetic fields and estimated upper critical fields.

| | 33.6 GPa | | 37.5 GPa | | 42.3 GPa | |
|---|---|---|---|---|---|---|
| | onset | 50% drop | onset | 50% drop | onset | 50% drop |
| Field (T) | $T$ (K) | | | | | |
| 0 | 4.94 | 4.05 | 5.24 | 4.33 | 5.37 | 4.64 |
| 0.5 | 4.5 | 3.62 | 4.713 | 3.91 | 4.822 | 4.11 |
| 1 | 4.03 | 3.29 | 4.296 | 3.5 | 4.254 | 3.66 |
| 1.5 | 3.65 | 2.97 | 3.833 | 3.2 | 3.791 | 3.26 |
| 2 | 3.28 | 2.64 | 3.474 | 2.85 | 3.349 | 2.81 |
| 2.5 | - | - | 3.08 | 2.49 | 2.984 | 2.42 |
| 3 | 2.57 | 1.98 | 2.72 | 2.04 | 2.57 | 1.99 |
| | $H_{c2}$ (0) (T) | | | | | |
| GL | 5.18 | 4.91 | 5.14 | 4.88 | 4.67 | 4.35 |
| WHH | | 4.83 | | 4.86 | | 4.26 |

**Figures:**

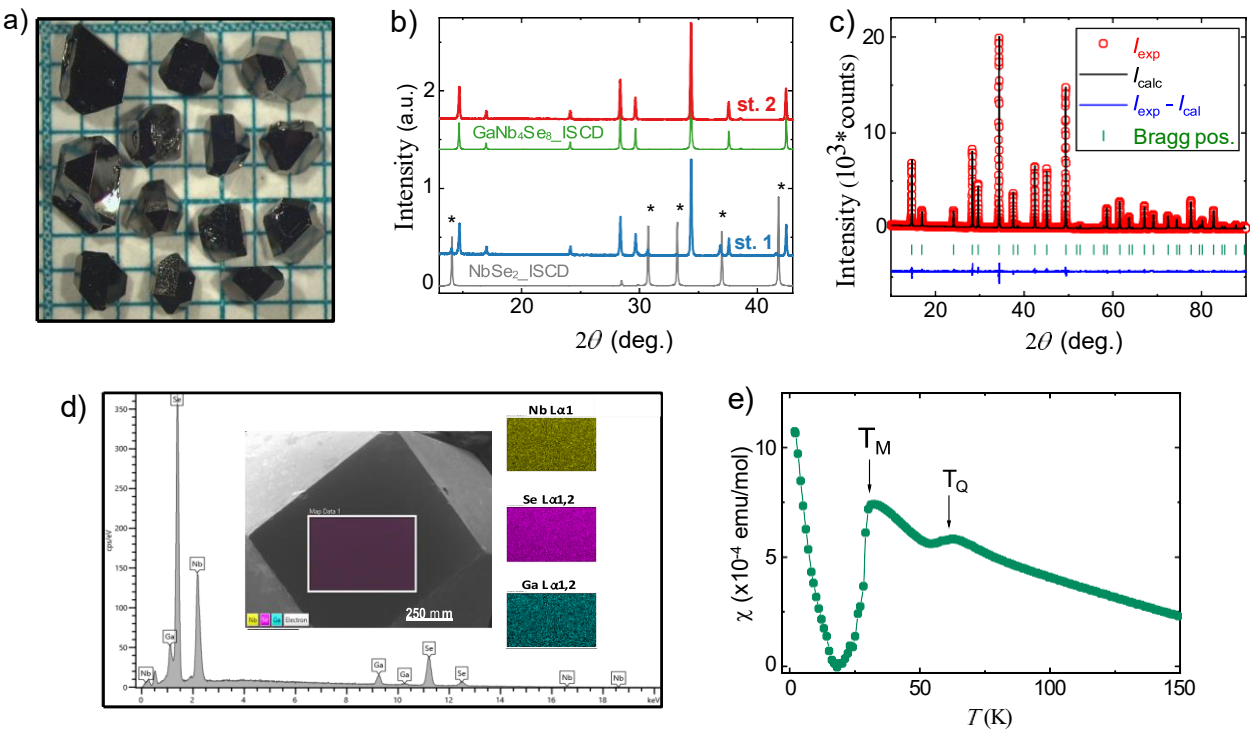


**Supplementary Figure S1. Crystal growth and characterization.** a) Optical image of as-grown $GaNb_4Se_8$ crystals showing well-defined (111) triangular and (001) rectangular facets. b) X-ray diffraction patterns of polycrystalline samples after the first (st.1) and second (st.2) sintering cycles, compared with reference patterns of $NbSe_2$ and $GaNb_4Se_8$ from the Inorganic Crystal Structure Database (ICSD, FIZ Karlsruhe). Asterisks mark diffraction peaks from the $NbSe_2$ impurity phase. c) Rietveld refinement of the st.2 sample confirming the formation of a single-phase cubic $GaNb_4Se_8$ (space group $F\bar{4}3m$). d) Energy-dispersive X-ray (EDS) spectrum acquired on the (001) surface of an as-grown $GaNb_4Se_8$ crystal. Insets show scanning electron microscopy (SEM) elemental maps illustrating the homogeneous chemical composition. e) Temperature dependence of magnetic susceptibility, showing distinct λ-type anomalies at the spin-singlet transition $T_M$ and the quadrupolar transition $T_Q$.

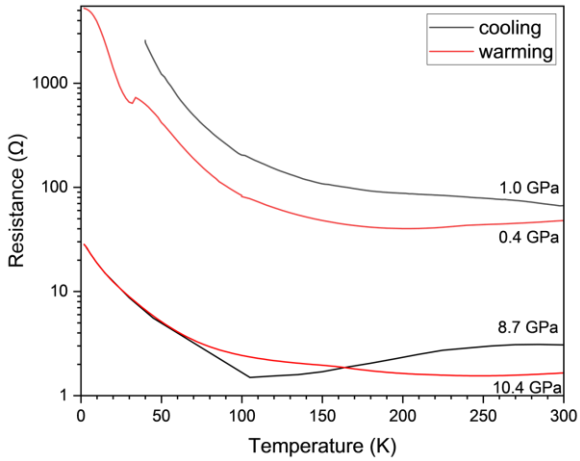


**Supplementary Figure S2.** Comparison of electrical transport data collected during cooling and warming cycles.

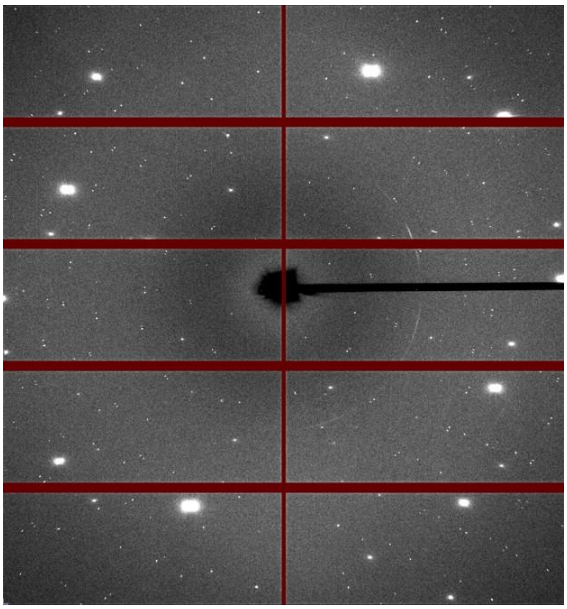

**Supplementary Figure S3.** Single-crystal diffraction pattern of $GaNb_4Se_8$ at ambient pressure. Red regions correspond to masked detector shadows.

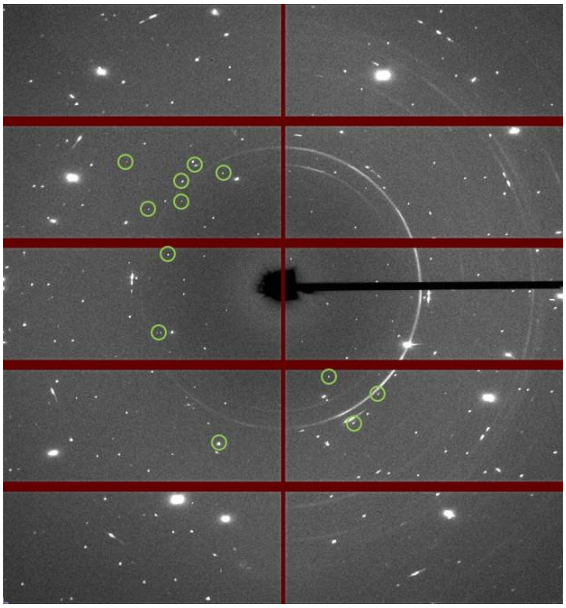

**Supplementary Figure S4.** Single-crystal diffraction pattern of $GaNb_4Se_8$ at 21.0 GPa. Green circles highlight the diffraction spots emerging from the new phase.

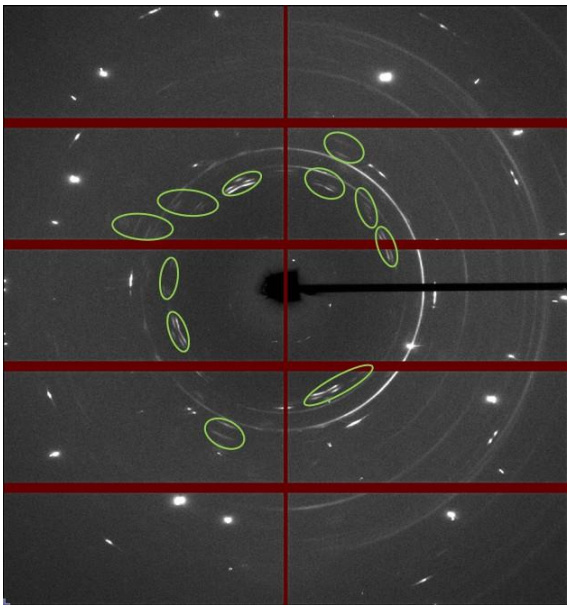

**Supplementary Figure S5.** Diffraction pattern of $GaNb_4Se_8$ at 28.2 GPa. The crystal is crushed into powder under this pressure, and the green ellipses mark the diffraction reflections of the high-pressure phase.

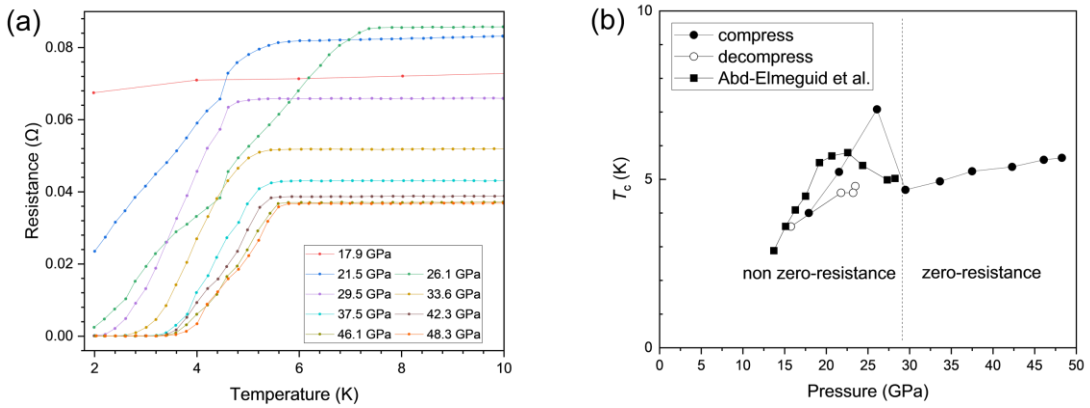


**Supplementary Figure S6.** (a) Temperature-dependent resistance of $GaNb_4Se_8$ measured between 2 and 10 K at pressures from 17.9 to 48.3 GPa. (b) Pressure dependence of the superconducting critical temperature ($T_c$). Temperature-dependent resistance at intermediate pressures, 17–26 GPa, showing filamentary superconductivity.

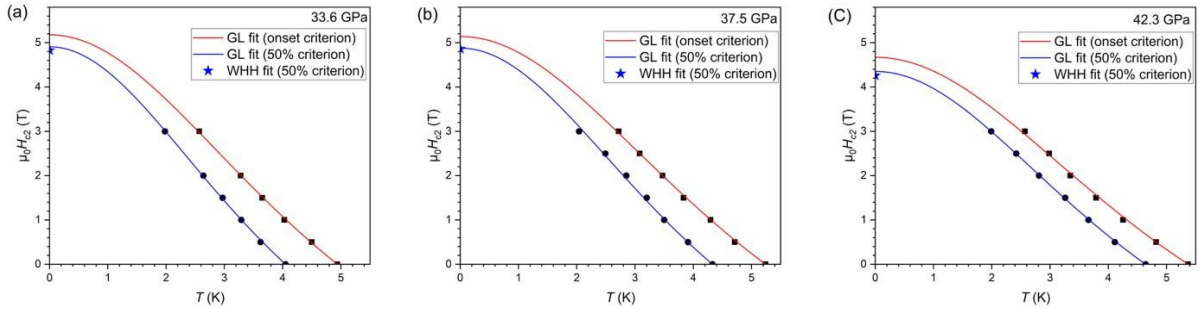


**Supplementary Figure S7.** Estimation of the upper critical magnetic field ($\mu_0 Hc_2$) at 33.6 (a), 37.5 (b), and 42.3 GPa (c). The critical superconducting transition temperatures (Tc) at different magnetic fields were fitted using the Ginzburg–Landau (GL) and Werthamer–Helfand–Hohenberg (WHH) models. Square and circle symbols denote Tc values determined from the onset of the resistance drop and the 50% resistance-drop criterion, respectively.